Macromolecular Nanotechnology

Electrospinning fabrication of partially crystalline bisphenol A polycarbonate nanofibers: Effects on conformation, crystallinity, and mechanical properties

Chia-Chun Liao [a], Cheng-Chien Wang [b], Kuo-Chen Shih [c], Chuh-Yung Chen [a],*

[a] Department of Chemical Engineering, National Cheng Kung University, 70101 Tainan, Taiwan
[b] Department of Chemical and Materials Engineering, Southern Taiwan University, 71005 Tainan, Taiwan
[c] Department of Optical-Grade Organic Materials, Nanopowder and Thin Film Technology Center, ITRI, 70995 Tainan, Taiwan

ARTICLE INFO

ABSTRACT

The application of an electrostatic and centrifugal field (1800 rpm) in a novel electrospinning process was shown to improve the degree of uniaxial alignment in polymer nanofibers and to enhance orientational order in polymer chains, producing bisphenol A polycarbonate (BPAPC) nanofibers with superior mechanical properties. High-speed videography showed that the additional centrifugal field effectively removed electrical bending instability and promoted molecular orientation during the electrospinning process. Infrared spectroscopic (IR) characterization revealed that the fraction of trans–trans conformers in BPAPC nanofibers reached 67% under optimal electrospinning conditions (25 kV and 1800 rpm at 25 °C). Modulated differential scanning calorimetry (MDSC) and wide-angle X-ray diffraction (WXRD) assays showed that a degree of crystallinity of 6.5% could be achieved. Moreover, two crystal phases at angles of $2\theta = 17.3°$ and $21.9°$ were produced in BPAPC nanofibers. The elastic modulus of BPAPC nanofibers with a crystallinity of 6.5% was 7.11 and 5.13 GPa, as measured via atomic force microscopy (AFM) and nanoindenter (NI) experiments, respectively. These results demonstrated that the mechanical behavior of BPAPC nanofibers could be improved by conducting the proposed electrospinning technique. Moreover, BPAPC nanofibers produced through the proposed method could be potentially applied for the reinforcement of composites.

Crown Copyright © 2011 Published by Elsevier Ltd. All rights reserved.

1. Introduction

Recent developments in nanotechnology have allowed materials and devices to be fabricated at the submicro- and nanoscale level. Miniaturization is a desirable process due to the superior mechanical properties [1] of nanoscale materials. To date, nanofibers have been used in applications such as tissue engineering [2], filter media [3], composite reinforcement [4–6], and micro- and nanoelectromechanical systems [7]. Electrospinning [8,9] has been recognized as an effective technique for the fabrication of polymeric nanofibers.

Bisphenol A polycarbonate (BPAPC) has been widely used as a high-performance engineering polymer due to its excellent toughness, weatherability, and transparency. Thus, BPAPC nanofibers have a high potential for the reinforcement of composites. Recently, many studies have reported the use of electrospinning techniques for the fabrication of BPAPC nanofibers [10–22]. Among these reports, the maximum modulus of BPAPC nanofibers was only 1.9 GPa [22].

BPAPC is an amorphous polymer due to the rigid nature of the molecular backbone. Recently, annealing techniques [23], organic solvents [24], vapors [25], vapor-grown

* Corresponding author. Tel.: +886 6 2360468; fax: +886 6 2344496.
E-mail address: ccy7@ccmail.ncku.edu.tw (C.-Y. Chen).

carbon fibers (VGCF) [26], supercritical carbon dioxide (SCCO$_2$) [27], and nanoscale fillers [28] have been applied to induce the crystallization of BPAPC and improve its mechanical properties. For example, by conducting a 24-h annealing technique, Von Falkai and Rellensman [23] obtained the first crystallites of BPAPC. Unfortunately, to develop a complete spherulite of BPAPC, the annealing process must be conducted for 1 week at 190 °C. However, organic solvents [24] and vapors [25] can be used to accelerate BPAPC crystallization and shorten the induction period. Furthermore, Takahashi et al. [26] reported that the crystallization of BPAPC was substantially accelerated by the introduction of a VGCF (5 wt.%) filler. Hu and Lesser [27] found that the degree of crystallinity of a thick BPAPC film (30 µm) was 26% after treatment at 95 °C and 3000 psi in the presence of SCCO$_2$ for 8 h. Yin et al. [28] induced the crystallization of amorphous BPAPC (heat of fusion = 29 J/g) by annealing the polymer at 200 °C for 10 h in the presence of a synergistic blend of a liquid–crystalline polymer (LCP) dispersed phase and a reactive compatibilizer (ethylene–methyl acrylate–glycidyl methacrylate copolymer (E–MA–GMA)). Although the aforementioned methods [23–28] can be used to prepare partially crystalline BPAPC, these processes require complicated procedures.

To the best of our knowledge, the degree of crystallinity of BPAPC nanofibers fabricated by electrospinning techniques has not been previously discussed. Therefore, in this study, partially crystalline BPAPC nanofibers with superior mechanical properties were fabricated via a novel electrospinning technique. This technique can effectively promote the orientation of locally parallel chain segments of BPAPC nanofibers via an electrostatic and centrifugal field (1800 rpm). Moreover, the conformation, crystallinity, and mechanical properties of the partially crystalline BPAPC nanofibers were investigated by field-emission scanning electron microscopy (FE–SEM), high-speed camera (CCD), infrared spectroscopy (IR), modulated differential scanning calorimetry (MDSC), wide-angle X-ray diffraction (WXRD), atomic force microscopy (AFM), and nanoindenter (NI) assays.

2. Experimental

2.1. Materials

All reagents were used without further purification. BPAPC resin pellets with an average molecular weight of $M_w = 1.68 \times 10^5$ g/mol (Chi-Lin Technology Co., Ltd) were dissolved in dichloromethane (CH$_2$Cl$_2$, Aldrich Co. Ltd.), chloroform (CHCl$_3$, Aldrich Co. Ltd.), or tetrahydrofuran (THF, Aldrich Co. Ltd.) to prepare 10, 12, and 14 wt.% solutions, respectively. To prepare solutions with different concentrations of BPAPC, appropriate amounts of the polymer and solvent were mixed for 7–8 h (25 °C) until homogeneous solutions were obtained. The properties of the solutions were measured at 25 °C (as shown in Table 1), and the viscosity and surface tension of the prepared solutions were measured with a viscosity meter (AND Vibro-Viscometer SV-10, range: 0.3–10,000 mPa s) and a surface-tension meter (FACE surface tensiometer CBVP-A3), respectively.

2.2. Electrospinning setup

Fig. 1 shows a schematic diagram of the novel electrospinning technique. A polymer solution was placed into a 50-mL syringe attached to a horizontally mounted syringe pump (kdSentificent KDS-100). A jacket-type heat exchanger was used to maintain the polymer solution at the desired temperature. The temperature of the pendant drop at the end of the needle of the PTFE tube (outer diameter = 6 cm) was measured using a thermocouple to determine the working temperature of the electrospinning process. The potential was applied to the upper surface of the PTFE tube using a high-voltage power supply (Pebio CE.LIF). Voltage was conducted via an interior copper pipe that ran through the upper surface of the PTFE tube to the end of the needle. A grounded copper ring (inner diameter = 50 cm) was used as the target. The spinning conditions for each polymer solution are provided in Tables 1 and 2.

2.3. Analysis

A Hitachi model S4200 field-emission scanning electron microscope (FE–SEM) was used to examine the diameter and morphology of the BPAPC nanofibers. A high-speed charge-coupled device (CCD; IDT XS-4) camera was used to observe the liquid jet emitted from the bottom of the Taylor cone. Images were captured at a rate of 5000 frame/s. Infrared spectra were recorded on a Varian 2000 FT-IR instrument under standard operating conditions. Each spectrum was calculated as the average of 32 scans at a resolution of 4 cm^{-1}. A conformationally sensitive in-plane aromatic group-stretching vibration at 1600 cm^{-1} was observed in the BPAPC samples [29]. This band contained clearly identifiable contributions from *trans–trans* and *trans–cis* conformers at approximately 1594 and 1604 cm^{-1}, respectively. Specific regions of the spectra (1500–1700 cm^{-1}) were analyzed individually using a commercially available curve-fitting program that was adapted to evaluate spectroscopic data (PeakFit).

Modulated differential-scanning calorimetry (MDSC) measurements were conducted on a TA Instruments Q2000 Modulated DSC. Samples were heated from 25 to 300 °C at a rate of 5 °C/min, and a 100-s modulation and a 1.326 °C modulation-temperature amplitude were applied. The MDSC assay used two simultaneous linear and sinusoidal heating rates. The MDSC sinusoidal heating rate allows for the separation of the total DSC heat-flow signal into two components, including a reversible component, which includes the heat capacity and accounts for a majority of the melting activity, and a nonreversible component, which includes the enthalpies of relaxation and thermoset curing. The degree of crystallinity was calculated by assuming that the heat of fusion of 100% crystalline BPAPC was 26.2 cal/g [27]. Wide angle X-ray diffraction (WXRD) patterns were recorded on a Rigaku ATX-E diffractometer equipped with a graphite-monochromated Cu K$_\alpha$ radiation source ($\lambda = 0.15405$ nm) operated at 30 mA and 40 kV from 10° to 40°.

The elastic properties of submicro- and nanofibers can be measured with a three-point bend test, where a single

Table 1
Preparation and characterization of solutions containing 10, 12, and 14 wt.% BPAPC in CH_2Cl_2, $CHCl_3$, or THF.

Sample symbol	BPAPC	CH_2Cl_2	$CHCl_3$	THF	Weight percent	Viscosity	Surface tension	Nanofiber Diameter[a]	Standard deviation[a]	Crystallinity[b]
	Weight (g)				(wt.%)	(cP)	(mN/m)	(nm)	(nm)	(%)
BPAPC-a	10	90		10		37.3	28.4	1,536	±123	0
BPAPC-b	12	88		12		127.0	30.1	2,718	±182	0
BPAPC-c	14	86		14		148.0	30.3	4,314	±211	0
BPAPC-d	10		90	10		101.0	28.7	1,592	±58	0
BPAPC-e	12		88	12		141.0	29.5	967	±50	0
BPAPC-f	14		86	14		332.0	32.8	1,407	±44	0
BPAPC-g	10			90	10	29.5	27.8	871	±37	0.9
BPAPC-h	12			88	12	30.8	27.9	672	±25	2.1
BPAPC-i	14			86	14	48.1	28.2	221	±12	6.5
BPAPC-j[c]	10			90	10	29.5	27.8	Beads	–	0
BPAPC-k[c]	12			88	12	30.8	27.9	Beads	–	0
BPAPC-l[c]	14			86	14	48.1	28.2	Beads	–	0

[a] BPAPC nanofibers were fabricated at a temperature of 25 °C, a flow rate of 0.25 mL/h, a spinneret tip-to-collector distance of 20 cm, an electrical field of 25 kV, and a centrifugal field of 1800 rpm. The nanofiber diameter displayed in each sample was calculated as the average of 40 fibers.
[b] The degree of crystallinity of the partially crystalline BPAPC nanofibers was measured by MDSC.
[c] BPAPC nanofibers were fabricated at a temperature of 25 °C, a flow rate of 0.25 mL/h, a spinneret tip-to-collector distance of 20 cm, and an electrical field of 25 kV in the absence of an additional centrifugal field.

nanofiber is suspended over an empty space and a small deflection is applied to the middle of the nanofiber along its length with an atomic-force microscope cantilever (Agilent Technologies P+ PicoPlus) in contact mode [30,31]. A schematic diagram of the three-point bend test and AFM-scanned cross-sectional profiles are provided in Fig. 2a–f. The three-point bend test can determine the mechanical properties of a single nanofiber by the direct determination of the applied force as a function of the displacement [30].

The maximum applied force (F) was calculated by constructing a force curve, which is a plot of the cantilever deflection (δ) as a function of sample position along the Z-axis. The force (F) applied by the AFM cantilever to the surface of the tip was calculated using Hooke's Law, where k is the force constant (0.2 N/m) and d is the movement of the piezo on the Z-axis. A simple relationship between F, k, and d is shown in Eq. (1).

$$F = k \cdot d \tag{1}$$

Using beam-bending theory [30], the modulus of a single nanofiber was calculated according to Eq. (2), where E is the elastic (Young's) modulus, L is the suspended length, and I is the second moment area of the beam. The value of I can be obtained from Eq. (3), where D is the beam diameter.

$$E = \frac{F \cdot L^3}{192 \cdot \delta \cdot I} \tag{2}$$

$$I = \frac{\pi \cdot D^4}{64} \tag{3}$$

To confirm the accuracy of the three-point bend test, the elastic–plastic nanoindentation test [32,33] was conducted to determine the hardness (H) and reduced elastic (Young's) modulus (E_r) of the near-surface region of the material. The MTS-Nanoindenter-XP (MTS-XP) apparatus uses a compliance indentation system capable of operating at loads in the microgram range, and the theoretical reso-

lution of the instrument is in the sub-nanoscale range. The indenter consists of a rod with a diamond tip (Berkovich) attached to the bottom. The resultant loading–unloading curves are often analyzed according to the Oliver–Pharr method [34]. In this study, the hardness was defined as:

$$H = \frac{P_{max}}{A} \tag{4}$$

where P_{max} is the load and A is the projected contact area at the depth of maximum penetration. For a normal Berkovich tip, the contact area is $A = 24.5 \times h^2$, and the contact depth is given by $h = h_{max} - \varepsilon \times P_{max}/S$, where h_{max} is the maximum contact depth, ε is the indenter geometry constant (0.75 or 0.76 [35]), and S is the stiffness. The value of S, which defines the E_r of the sample and is obtained from the unloading-curve slope, was calculated according to Eq. (5), where β is the corrected coefficient of the Berkovich probe (1.034 [34]):

$$S = \beta \frac{2}{\sqrt{\pi}} E_r \sqrt{A} \tag{5}$$

The elastic modulus of the sample (E_s) and the Poisson ratio ($v_s = 0.33$) were obtained according to Eq. (6):

$$\frac{1}{E_r} = \frac{1 - v_s^2}{E_s} + \frac{1 - v_i^2}{E_i} \tag{6}$$

where E_i and v_i are the elastic modulus and Poisson's ratio of the diamond indenter, respectively ($E_i = 1140$ GPa, $v_i = 0.07$ [36–40]).

3. Results and discussion

3.1. BPAPC nanofiber fabrication process

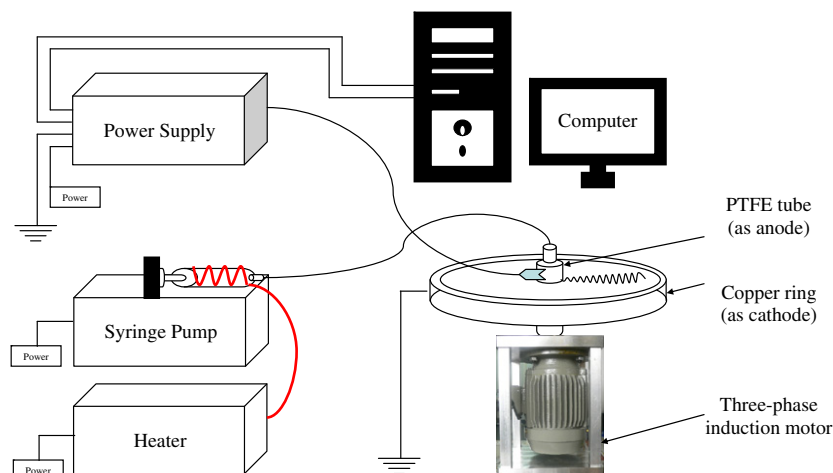The morphology of the polymeric nanofibers was strongly dependent on the parameters of the electrospin-

Fig. 1. Schematic depiction of the proposed electrospinning technique used for the preparation of partially crystalline BPAPC nanofibers.

ning processing, including the solvent type, solution concentration, electrostatic field, and solution temperature, as shown in previous studies [8]. In this study, the effects of these parameters on the conformation, crystallinity, and mechanical properties of BPAPC nanofibers were further investigated.

3.1.1. Effect of solution properties

As shown in our previous study [41], the physical properties of the solvents play an important role in the electrospinning process. Eight organic solvents including $CHCl_3$, CH_2Cl_2, THF, chlorobenzene (C_6H_5Cl), 1,2-dichloroethane ($C_2H_4Cl_2$), 1,1,2,2-tetrachloroethane ($C_2H_2Cl_4$), 1,1,2,2-tetrachloroethylene (C_2Cl_4) and N,N-dimethylformamide (DMF) were employed as carrier solvents in the preparation of BPAPC nanofibers. However, BPAPC would not completely dissolve in C_6H_5Cl, C_2Cl_4, or DMF. Moreover, BPAPC could not be electrospun in $C_2H_4Cl_2$ or $C_2H_2Cl_4$ because the viscosity of the solution was too high, and pipeline blockage occurred. Among these solvents, only $CHCl_3$, CH_2Cl_2, and THF could be successfully applied as carrier solvents to obtain high-quality BPAPC nanofibers.

The concentration of BPAPC in CH_2Cl_2, $CHCl_3$, and THF was varied (10, 12, or 14 wt.%) to study the effects of BPAPC concentration on the morphology and crystallinity of BPAPC nanofibers. The spinning parameters used in each experiment are shown in Table 1. The results indicated that the boiling point (b_p) and the viscosity of BPAPC solutions were highly dependent on the solvent. Fig. 3a–d present the FE–SEM images and two plots of BPAPC nanofibers fabricated from **BPAPC-a**. The results indicated that the solution with the lowest viscosity (37.3 cp, **BPAPC-a**) produced nanofibers with a uniform morphology and diameter. Most of the fibers distributed at a diameter range of 2000–2500 nm (Fig. 3c) and the diameter ranges of 1000–2500 nm have a larger gap of error bars (Fig. 3d) due to the lower b_p. In this study, an additional centrifugal field applied to an electrostatic field produced a strong stretching force, this strong stretching force could not be continuously stretched and thinned due to the rapid evaporation of solvent (the b_p of CH_2Cl_2 ~40 °C). Alternatively, the solution with the highest viscos-

ity (148.0 cp, **BPAPC-c**) produced irregular beads with single nanofibers containing varying diameters, as shown in Supporting information. Moreover, chain entanglement significantly increased with an increase in the solution concentration and viscosity [42]. However, when the highest viscosity solution was employed (148.0 cp, **BPAPC-c**), the stretching of entangled molecules under elongational flow was reduced, producing a beads-on-a-string structure [43] and numerous beaded nanofibers. Fig. 3e–l exhibit the FE–SEM images and four plots of BPAPC nanofibers fabricated from **BPAPC-d** and **BPAPC-e**, respectively. Most of the fibers distributed at diameter ranges of 800–1200 nm (Fig. 3k) and the diameter ranges of 400–1600 nm both have a smaller gap of error bars (Fig. 3l) when the b_p of solvent controlled effectively. As shown in Fig. 3e and f, the solution with the lowest viscosity (101.0 cp, **BPAPC-d**) produced irregular beads and beaded nanofibers. Alternatively, the flow rate of the polymer solution with the highest viscosity was extremely unstable (332.0 cp, **BPAPC-f**), resulting in the formation of beaded nanofibers (Supporting information). In this study, an additional centrifugal field can effectively remove the bending stability of electrically charged liquid jets and to fabricate aligned and molecularly oriented nanofibers dependent on the rate of solvent evaporation. When an additional centrifugal field applied an electrostatic field can produce a strong stretching force and further accelerate the rate of solvent evaporation. When the lower boiling point (b_p) solvent (CH_2Cl_2 ~40 °C) was executed, **BPAPC-a**, **BPAPC-b**, and **BPAPC-c** have not the formation of pores due to the rapid evaporation of solvent during the electrospinning process. Similarly, the higher boiling point (b_p) solvent (THF ~66 °C) was executed; **BPAPC-g**, **BPAPC-h**, and **BPAPC-i** also have not the formation of pores when the b_p of solvent controlled effectively during the electrospinning process. However, when the higher b_p solvent ($CHCl_3$ ~61 °C) was executed, porous fibers can be noted in **BPAPC-d** (Fig. 3e and f) and **BPAPC-f** (Supporting information), the phase separation occurs into solvent-rich and solvent-poor regions under a strong stretching force. Greiner and Wendorff [44] pointed that different fiber topologies were generated by choosing particular solvents, solvent mixtures, polymer

Table 2

The physical properties of partially crystalline BPAPC nanofibers fabricated from 14 wt.% BPAPC/THF solution under different operating conditions.

Operational variables[a]		Diameter[b]	trans–trans[c]	T_m[d]	Crystallinity[e]	X_{angle}[f]	Modulus[g]	Modulus/hardness[h]
		(nm)	(%)	(°C)	(%)	(°)	(GPa)	(GPa)
25 °C	5 kV	1,484	52	220	2.1	17.3; 21.9	0.01	0.52/0.01
	10 kV	992	52	221	2.2	17.3; 21.9	0.04	1.61/0.21
	15 kV	526	57	223	2.4	17.3; 21.9	0.52	3.05/0.21
	20 kV	366	59	224	4.3	17.3; 21.9	2.86	3.93/0.39
	25 kV	270	67	225	6.5	17.3; 21.9	7.11	5.13/0.52
	30 kV	340	61	224	3.0	17.3; 21.9	2.11	2.77/0.32
25 kV	25 °C	270	67	225	6.5	17.3; 21.9	7.11	5.13/0.52
	30 °C	2,482	52	222; 244	1.8	17.3; 21.9	1.11×10^{-3}	–
	35 °C	3,949	48	225; 246	1.7	21.9	1.58×10^{-4}	–
	40 °C	4,719	49	225; 246	1.5	21.9	9.89×10^{-5}	–
	45 °C	12,856	49	226; 246	1.4	21.9	1.70×10^{-6}	–

[a] BPAPC nanofibers were fabricated at a flow rate of 0.25 mL/h and a spinneret tip-to-collector distance of 20 cm under a centrifugal field (1800 rpm). The diameter of the nanofiber was calculated as the average of 30 fibers.

[b] Measured by FE–SEM.

[c] The ratio of the trans–trans conformer of partially crystalline BPAPC nanofibers was measured by PeakFit.

[d] T_m, melting temperature obtained from DSC.

[e] The degree of crystallinity of partially crystalline BPAPC nanofibers was measured by MDSC.

[f] X_{angle}, diffraction peaks obtained by WXRD.

[g] Measured by AFM.

[h] Measured by nanoindentation.

mixtures, or varying the humidity during the electrospinning process. For instance, phase separation occurs into polymer-rich and polymer-poor regions upon evaporation of the solvent, there is a high probability that pores will form in the solid in the polymer-poor region. Because the rate of solvent evaporation was limited under specific concentrations (**BPAPC-d** and **BPAPC-f**); the phase separation occurs into solvent-rich and solvent-poor regions for **BPAPC-d** due to residual solvent in nanofibers, and the phase separation occurs into polymer-rich and polymer-poor regions for **BPAPC-f** due to lack of solvent in nanofibers under a strong stretching force. Thus, when the higher b_p solvent (CHCl$_3$ ~61 °C) was executed, porous fibers can be noted in **BPAPC-d** (Fig. 3e and f) and **BPAPC-f** (Supporting information). Fig. 3m–p display the FE–SEM images and two plots of BPAPC nanofibers fabricated from **BPAPC-i**. Most of the fibers distributed at diameter ranges of 150–250 nm (Fig. 3o) and the diameter ranges of 100–450 nm both have a smaller gap of error bars (Fig. 3p) when the b_p of solvent controlled effectively. Notably, a mixture of BPAPC beads and nanofibers was obtained when the solution with the lowest viscosity (29.5 cp, **BPAPC-g**) was used (Supporting information). Beads and beaded nanofibers were less likely to be formed with more viscous solutions (30.8 cp, **BPAPC-h**), and the shape of the beads gradually changed from spherical to conical as the viscosity increased (Supporting information). With the most viscous solution (48.1 cp, **BPAPC-i**), uniaxially aligned BPAPC nanofibers were obtained (Fig. 3m and n). The above results (**BPAPC-d**, **BPAPC-g**, and **BPAPC-h**) indicated that beads and beaded nanofibers were formed due to the absence of chain entanglement. Alternatively, uniform nanofibers were formed under strong elongational flow at specific viscosities (**BPAPC-a**, **BPAPC-e**, and **BPAPC-i**). For instance, if the viscosity was too high, irregularly beaded nanofibers (**BPAPC-b**, **BPAPC-c**, and **BPAPC-f**)

were produced during the electrospinning process due to excess chain entanglement [42]. Particularly, it can be observed that **BPAPC-c** and **BPAPC-e** have about the same viscosity, but **BPAPC-e** yields fibers which are much more uniform and with less beads (Fig. 3i and j). In this study, an additional centrifugal field applied to an electrostatic field produced a strong stretching force, this strong stretching force could not be continuously stretched and thinned due to the rapid evaporation of solvent (the b_p of CH$_2$Cl$_2$ ~40 °C). Contrary, this strong stretching force could be continuously stretched and thinned the BPAPC fibers when the b_p of solvent controlled effectively (the b_p of THF ~66 °C). Fig. 3i–p reveal the degree of uniaxial alignment of BPAPC nanofibers was increased and the mean diameter of BPAPC nanofibers more uniform fabricated from the BPAPC dissolved in CHCl$_3$ and THF solutions, respectively. This result demonstrates that a strong stretching force can substantially promote the degree of uniaxial alignment of BPAPC nanofibers when the b_p of solvent controlled effectively.

As shown in Table 1, MDSC results indicated that **BPAPC-a** to **BPAPC-f** did not possess crystalline features and **BPAPC-g** to **BPAPC-i** displayed varying degrees of crystallinity. According to the calculation proposed by Hu and Lesser (2004) [27], the degree of crystallinity of **BPAPC-g**, **BPAPC-h, and BPAPC-i** were 0.9, 2.1, and 6.5, respectively. These results are consistent with those of our previous study [41], in which BPAPC formed a denser, worm-like chain conformation in THF, as determined by nuclear magnetic resonance (NMR), dynamic light scanning (DLS), and Raman spectroscopy. For comparison, a conventional electrospinning technique was used to fabricate BPAPC nanofibers under the same conditions, and the resulting fibers were labeled as **BPAPC-j**, **BPAPC-k**, and **BPAPC-l**, as shown in Table 1. However, with the conventional technique, all of the BPAPC solutions produced only
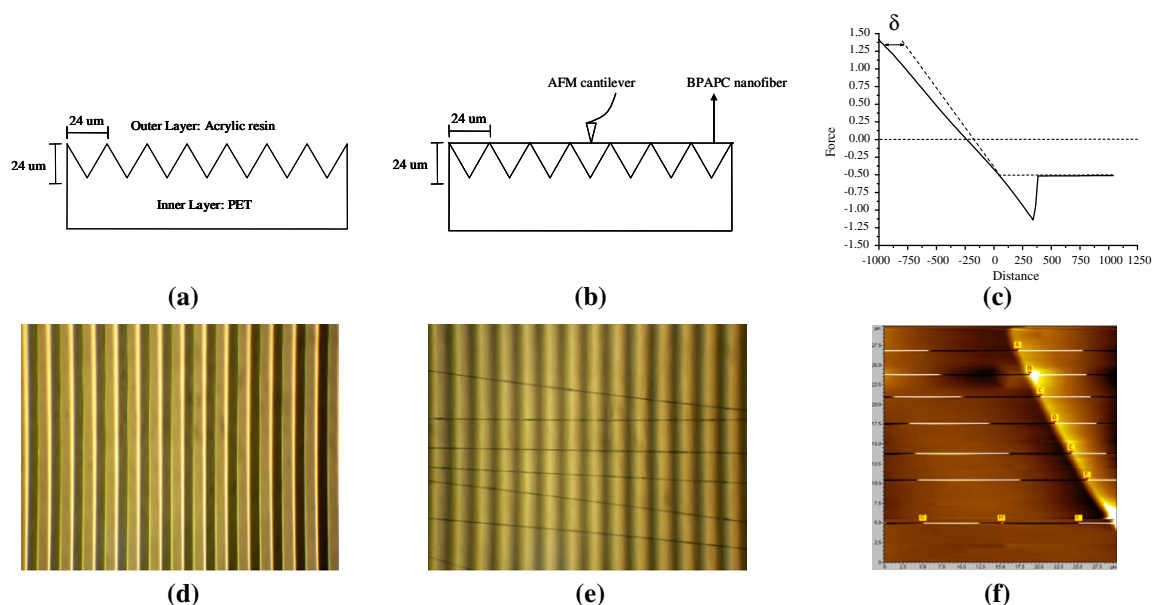
Fig. 2. Schematic diagrams of (a) the appearance and composition of the inner and outer layers of the support substrate, (b) the three-point bend test, which was conducted with an AFM probe, (c) a typical force-distance curve (the dotted line is the sample and the dashed line is the reference), (d) an OM image of the empty substrate, (e) an OM image of BPAPC nanofibers suspended over a substrate, and (f) AFM contact-mode image.

BPAPC beads without crystalline features (not shown for brevity). To reiterate, the electrostatic (25 kV) and centrifugal (1800 rpm) forces acting on the nanofibers tend to stretch and align the polymer chains, allowing the stretched nanofibers to remain in the stretched state. Consequently, the experimental results clearly demonstrated that an electrostatic and centrifugal field (1800 rpm) can effectively promote the orientation of locally parallel chain segments of BPAPC nanofibers.

3.1.2. Effect of operational parameters

A liquid droplet is attached to a needle by surface tension and viscoelastic stresses. When the electrostatic field of the surface of the pendant drop at the end of the needle is increased to a sufficiently high value, a charged jet of fluid is ejected. The diameter of the jet decreases as the distance from the needle decreases, and the thin jet of fluid solidifies into nanofibers [43]. Thus, the spinning electrostatic field plays a significant role in the structure and diameter of nanofibers. As shown in Table 2, the diameter of the nanofibers decreased from 1434 to 270 nm as the spinning electrostatic field increased from 5 to 25 kV. At lower electrostatic fields (5 kV), the force balance between repulsive forces and surface tension could not sufficiently stretch the nanofibers; however, as the electrostatic field increased to 25 kV, the nanofibers became thinner. As the solution jet moved towards the collector, the electrostatic field stretched the jet, and thinner nanofibers were produced [13]. Fig. 4a shows the tapered straight segment of a jet emanating from the droplet surface at a voltage of 25 kV. As shown in the figure, the jet was continuously elongated and thinned throughout the process. In the conventional electrospinning technique, bending perturbations were observed, and the filament rapidly grew into a

coil under the influence of the charged jet [43]. Unlike previous methods [10–22], a turning point at approximately 120° was observed in the proposed electrospinning technique. Due to the additional centrifugal field, the turning point replaced the bending perturbations (see Fig. 4a), and electrical bending instability disappeared (t = 0.2–2.4 ms). As a result, the jet became longer and thinner. To summarize, strong shear stress (25 kV and 1800 rpm) greatly enhanced the macroscopic elongation of the jet and the microscopic alignment of the nanofibers. The nanofibers remained in the stretched state, further promoting crystallinity. As a result, the thermal and mechanical properties of BPAPC nanofibers were improved due to the elimination of electrical bending instability. Hence, BPAPC nanofibers fabricated from **BPAPC-i** at 25 kV and 25 °C displayed a uniaxial alignment and a high aspect ratio (see Fig. 3m and n). Thus, the nanofibers produced by the proposed method were superior to those produced by other traditional electrospinning processes [10–22]. Alternatively, the diameter of the nanofibers increased from 270 to 340 nm as the spinning electrostatic field was further increased to 30 kV. According to Deitzel et al., increasing the electrostatic field creates instability in the originating surface of the pendant drop at the end of the needle and increases the density of the beads [45]. Thus, to obtain partially crystalline BPAPC nanofibers, an electrostatic field of 25 kV is optimal.

To study the effects of temperature on the properties of BPAPC nanofibers, the operating temperature was increased from 25 to 45 °C, and the results are shown in table 2. The diameter of the nanofibers increased from 270 to 12,856 nm as the temperature of the spinning solution increased from 25 to 45 °C. The observed increase in diameter was attributed to the accelerated rate of solvent
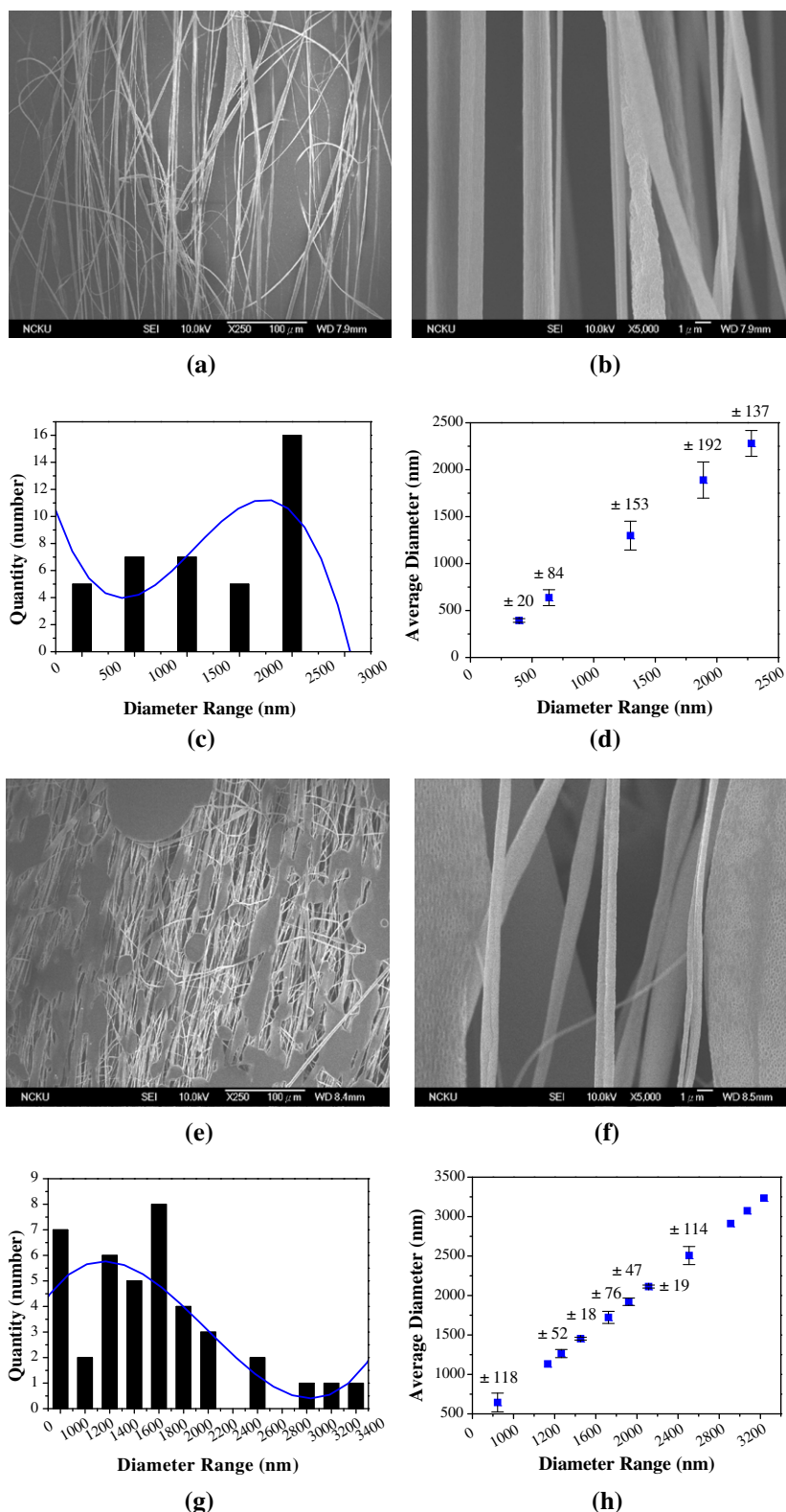
Fig. 3. FE–SEM images of BPAPC nanofibers prepared from (a and b) **BPAPC-a**, plot of (c) the quantity vs. the diameter range and (d) the average diameter vs. the diameter range; (e and f) **BPAPC-d**, plot of (g) the quantity vs. the diameter range and (h) the average diameter vs. the diameter range; (i and j) **BPAPC-e**, plot of (k) the quantity vs. the diameter range and (l) the average diameter vs. the diameter range; (m) and (n) **BPAPC-i**, plot of (o) the quantity vs. the diameter range and (p) the average diameter vs. the diameter range (The error in the readings is taken as the standard deviation of the normal distribution of nanofibers measured from the FE–SEM images).

MACROMOLECULAR NANOTECHNOLOGY

(i)

(j)

(k)

(l)

(m)

(n)

(o)
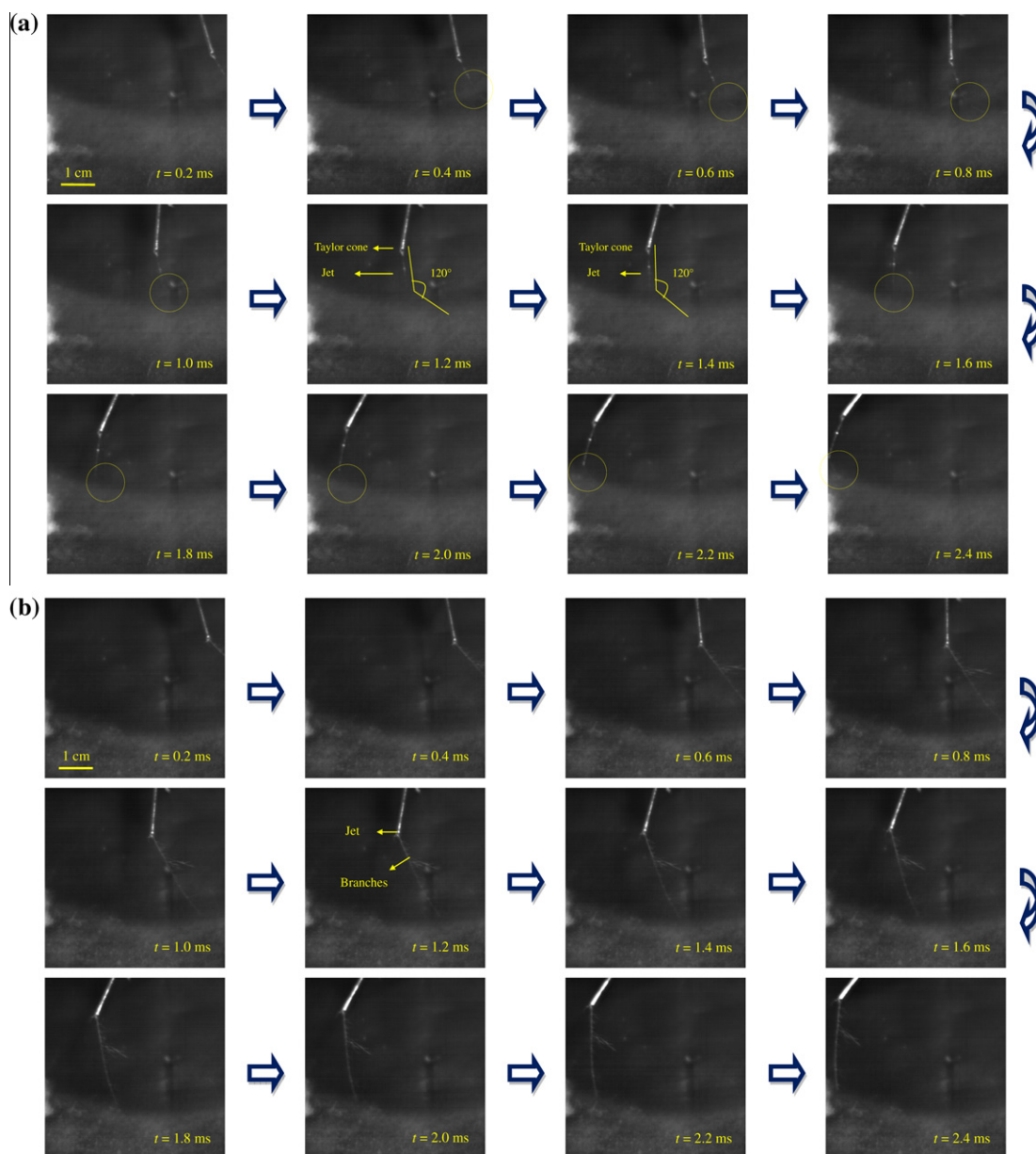

(p)
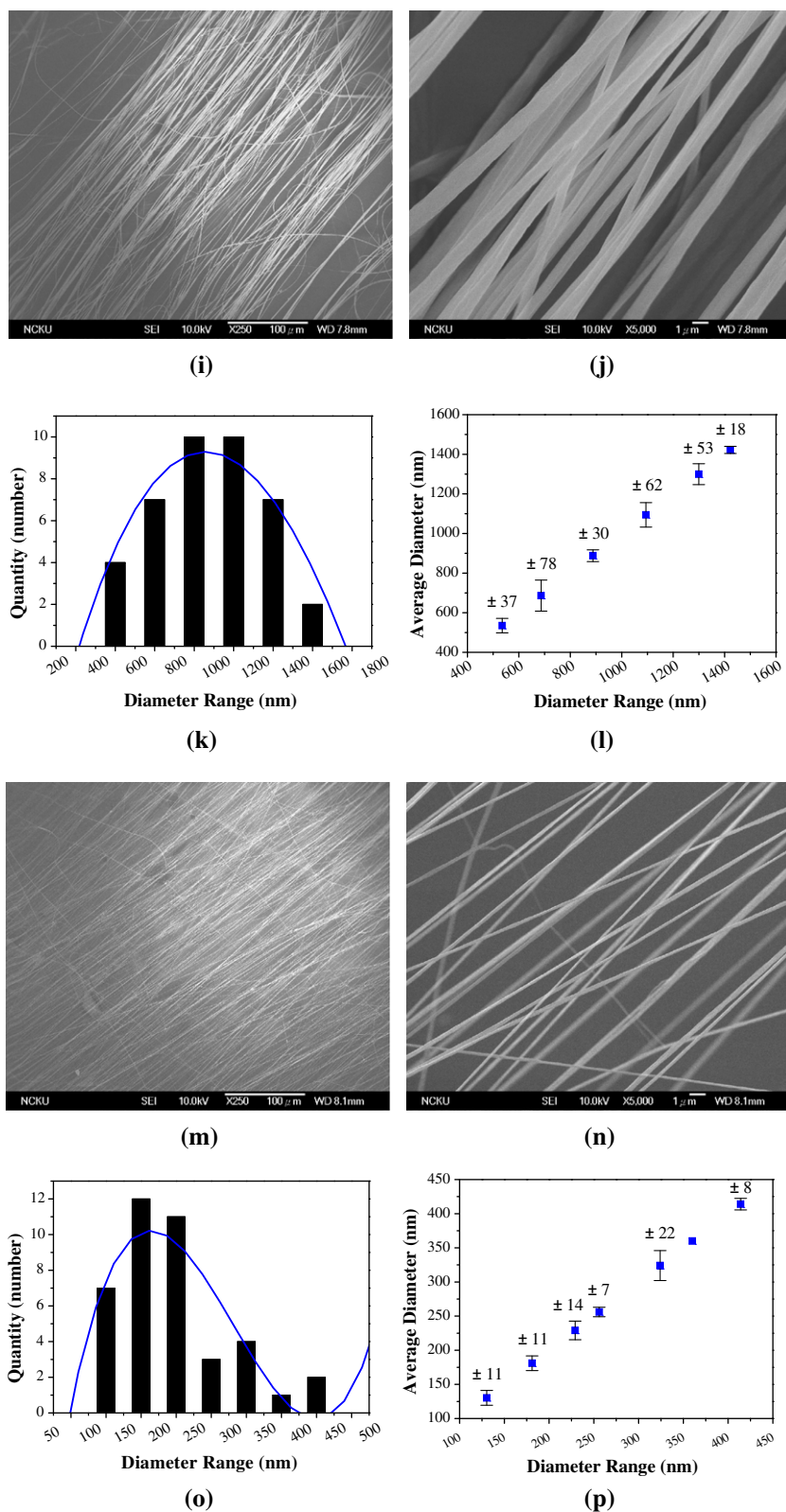
Fig. 3 (*continued*)

Fig. 4. (a) Evolution, growth, and downstream motion of a short segment of a jet of **BPAPC-i** at 25 kV and 25 °C. The middle frame (0.8 ms) shows a well-developed straight segment produced by electrostatic and centrifugal fields. (b) The middle frame (0.8 ms) displays the branches that grew along the straight segment of a jet of **BPAPC-i** at 25 kV and 45 °C. Branch growth was driven by the electrostatic field from the charged jet.

evaporation at higher temperatures, which leads to an increase in surface tension due to an increase in the solidification speed of the jet. As excess charge accumulated on the surface of the jet, an unexpected phenomenon may have occurred at the surface of the cylinder jet. This phenomenon grew large enough to cause significant instability, and branches grew outward from the cylinder jet, as shown in Fig. 4b. The images shown in Fig. 4b (*t* = 0.2–2.4 ms) indicated that branches possessing a large diameter could become long and entangled, and could solidify to form beaded nanofibers. Therefore, the diameter of the beaded nanofibers increased substantially as the temperature increased to 45 °C due to the accelerated rate of solvent evaporation [43]. However, the orientation of locally parallel chain segments of BPAPC nanofibers could also be enhanced due to increased mobility at high temperatures [46]. Thus, the conformation, crystallinity, and mechanical properties of nanofibers fabricated from **BPAPC-i** will be discussed in further detail.

3.2. Conformation of BPAPC nanofibers

The $C_{carbonate}$–O–$C_{phenylene}$ moiety of BPAPC chains can exist as *trans–trans* and *trans–cis* conformers due to π-flip-
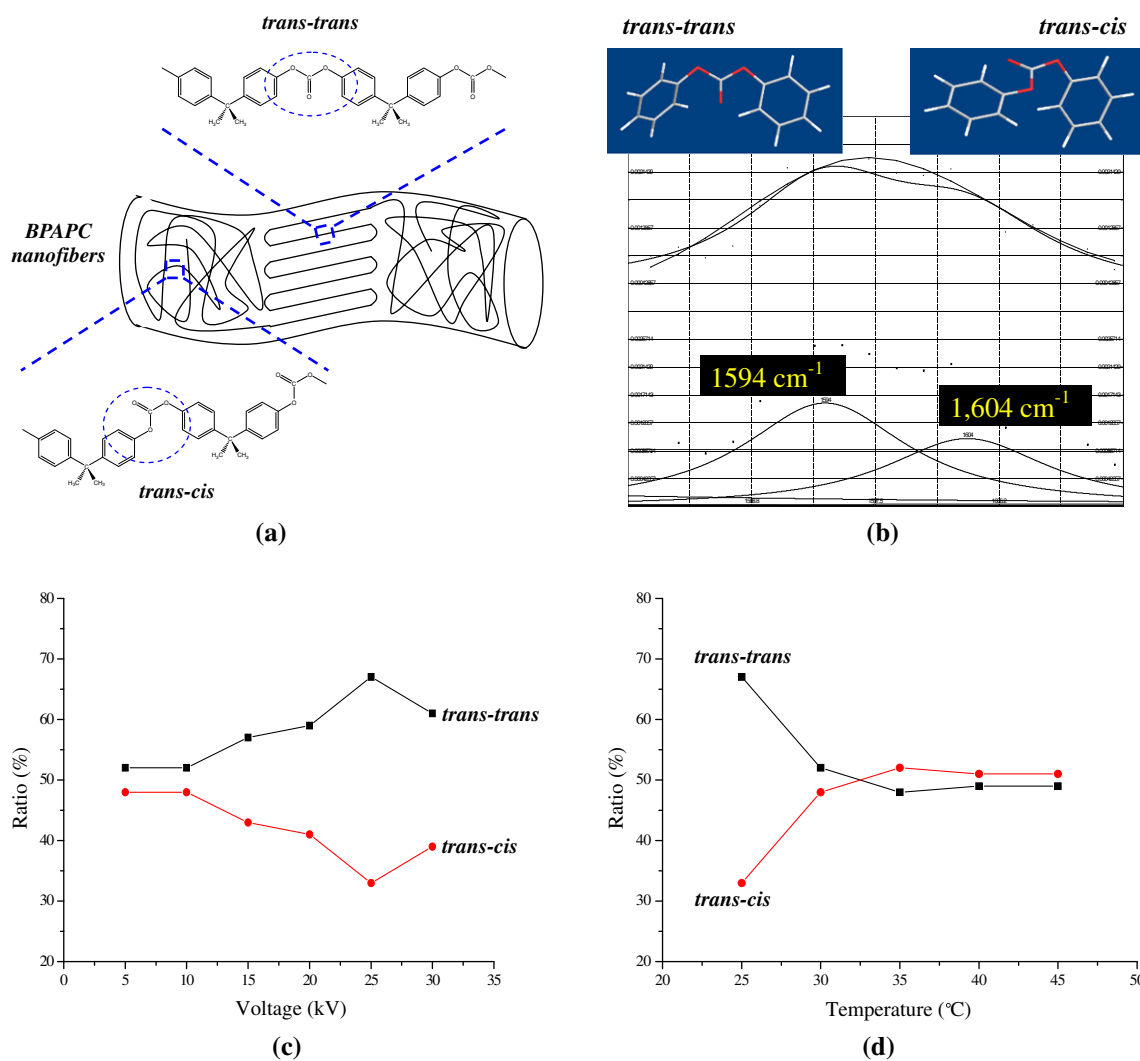
MACROMOLECULAR NANOTECHNOLOGY

Fig. 5. (a) A BPAPC chain showing *trans–trans* and *trans–cis* conformers in partially crystalline BPAPC nanofibers. (b) Curve fitting of the IR spectra between 1590 and 1605 cm^{-1}. The ratios of *trans–trans* and *trans–cis* conformers of **BPAPC-i** fibers prepared under different (c) electrostatic fields and (d) solution temperatures.
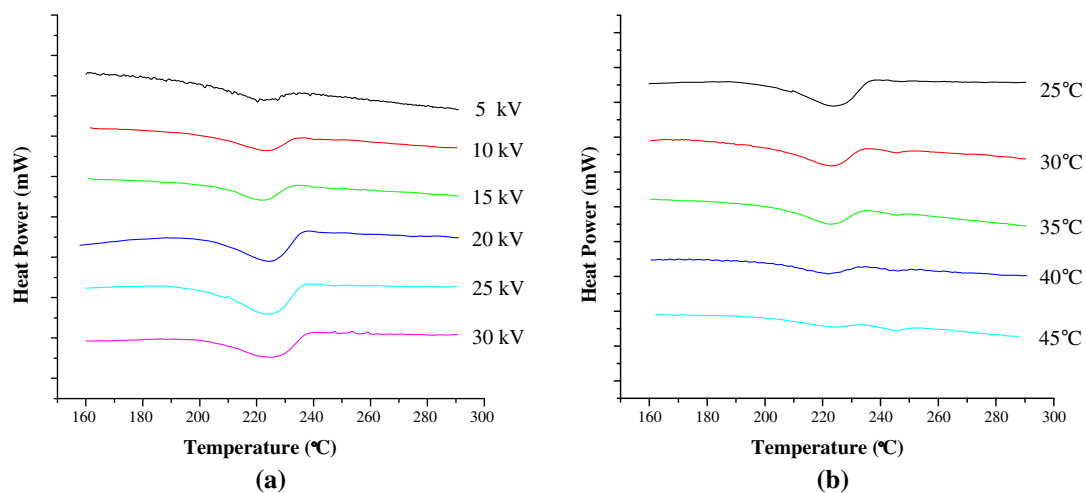

Fig. 6. The first-heating MDSC curves of **BPAPC-i** fibers prepared under different (a) electrostatic fields and (b) solution temperatures.
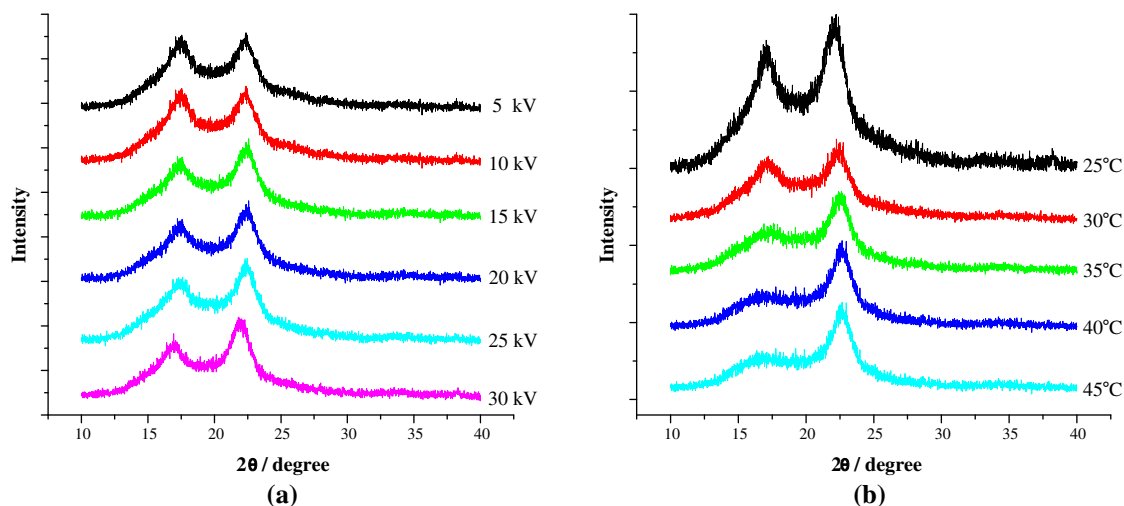
Fig. 7. The WXRD patterns recorded for **BPAPC-i** fibers prepared under different (a) electrostatic fields and (b) solution temperatures.
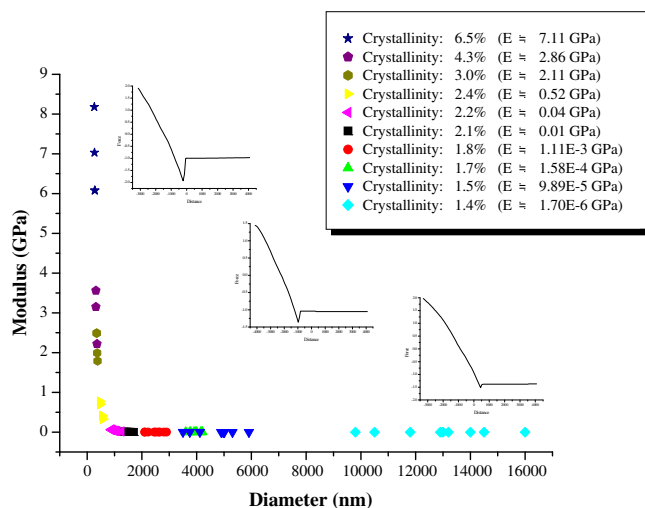

Fig. 8. The elastic modulus *vs.* diameter curves for **BPAPC-i** fibers with various degrees of crystallinity.

ping of the phenyl group [47] (shown in Fig. 5a). Both *trans–trans* and *trans–cis* conformers can exist in the amorphous phase. In the FT-IR spectrum of BPAPC, the bands at 1594 and 1604 cm^{-1} were assigned to C=O stretching vibrations in the *trans–trans* and *trans–cis* conformers, respectively (shown in Fig. 5b). The high-frequency band (1594 cm^{-1}) corresponds to the less energetically favorable *trans–trans* conformer, while the lower-frequency band (1604 cm^{-1}) corresponds to the energetically favored *trans–cis* conformer [48]. Thus, the deconvoluted IR absorption peaks can be used to monitor conformational changes of BPAPC nanofibers prepared under different electrostatic fields and operating temperatures. As shown in Fig. 5b, the characteristic peak of the $C_{carbonate}$–O–$C_{phenylene}$ moiety in **BPAPC-i** nanofibers was deconvoluted using the Lorentzian method, and the results indicated that the ratio of *trans–trans* to *trans–cis* conformers was 52/48,

52/48, 57/43, 59/41, 67/33, and 61/39 under an electrostatic field of 5, 10, 15, 20, 25, and 30 kV, respectively. At the lowest electrostatic field (5 kV), the *trans–trans* to *trans–cis* conformer ratio was only 52/48, which indicates that only a small number of polymer chains were aligned during the electrospinning process. In contrast, the *trans–trans* to *trans–cis* conformer ratio reached 67/33 at an electrostatic field of 25 kV, as shown in Fig. 5c. These results indicated that the shear force of a centrifugal field can induce the isomerization of the *trans–trans* conformer in the presence of a low or high electrostatic field. The lowest shear force required to isomerize the conformer was 5 kV and 1800 rpm, which suggested that polymer chains located along the nanofiber axis possessed a lower degree of misorientation and that higher shear forces (25 kV and 1800 rpm) induce molecular orientations parallel to the nanofiber axis. The experimental results also demonstrated that

that an electrostatic field with an additional centrifugal field (1800 rpm) can improve the alignment of polymer chains in the nanofibers and further align polymer chains parallel to the nanofiber axis [49,50]. Moreover, the trans–trans to trans–cis ratio of **BPAPC-i** at an operating temperature of 25, 30, 35, 40, and 45 °C was 67/33, 52/48, 48/52, 49/51, and 49/51, respectively. Thus, the ratio of elongated molecules greatly decreased as the temperature increased to 45 °C, which is consistent with the SEM results. Obviously, higher operating temperatures accelerate the rate of solvent evaporation and do not improve the orientation of locally parallel chain segments of BPAPC nanofibers, as shown in Fig. 5d.

3.3. Crystallinity of the BPAPC nanofibers

Fig. 6a shows the first heating MDSC curves of **BPAPC-i** nanofibers under electrostatic fields of 5, 10, 15, 20, 25, and 30 kV, respectively. Only the glass-transition temperature ($T_g \sim 145$ °C) was observed in the MDSC curve of pure

BPAPC, and endothermic peaks were not apparent [27]. However, an obvious endothermic peak ($T_m \sim 223$ °C) was present in the MDSC heating curve of BPAPC nanofibers. Based on the calculation proposed by Hu and Lesser (2004) [27], the degree of crystallinity of **BPAPC-i** nanofibers spun under electrostatic fields of 5, 10, 15, 20, 25, and 30 kV was 2.1, 2.2, 2.4, 4.3, 6.5, and 3.0, respectively. These results indicated that crystallinity can be induced in BPAPC nanofibers through the application of an electrostatic field and an additional centrifugal field (1800 rpm). Furthermore, the maximum crystallinity of **BPAPC-i** nanofibers fabricated at 25 kV and 25 °C was 6.5%, suggesting that an additional centrifugal field (1800 rpm) can effectively promote the orientation of locally parallel chain segments in BPAPC nanofibers during electrospinning. Fig. 6b shows the first heating MDSC curves of **BPAPC-i** nanofibers spun at 25, 30, 35, 40, and 45 °C, respectively. As the temperature of the solution increased, the endothermic peak at 223 °C in the MDSC heating curve decreased and a weak endothermic peak at 245 °C began to appear. This result
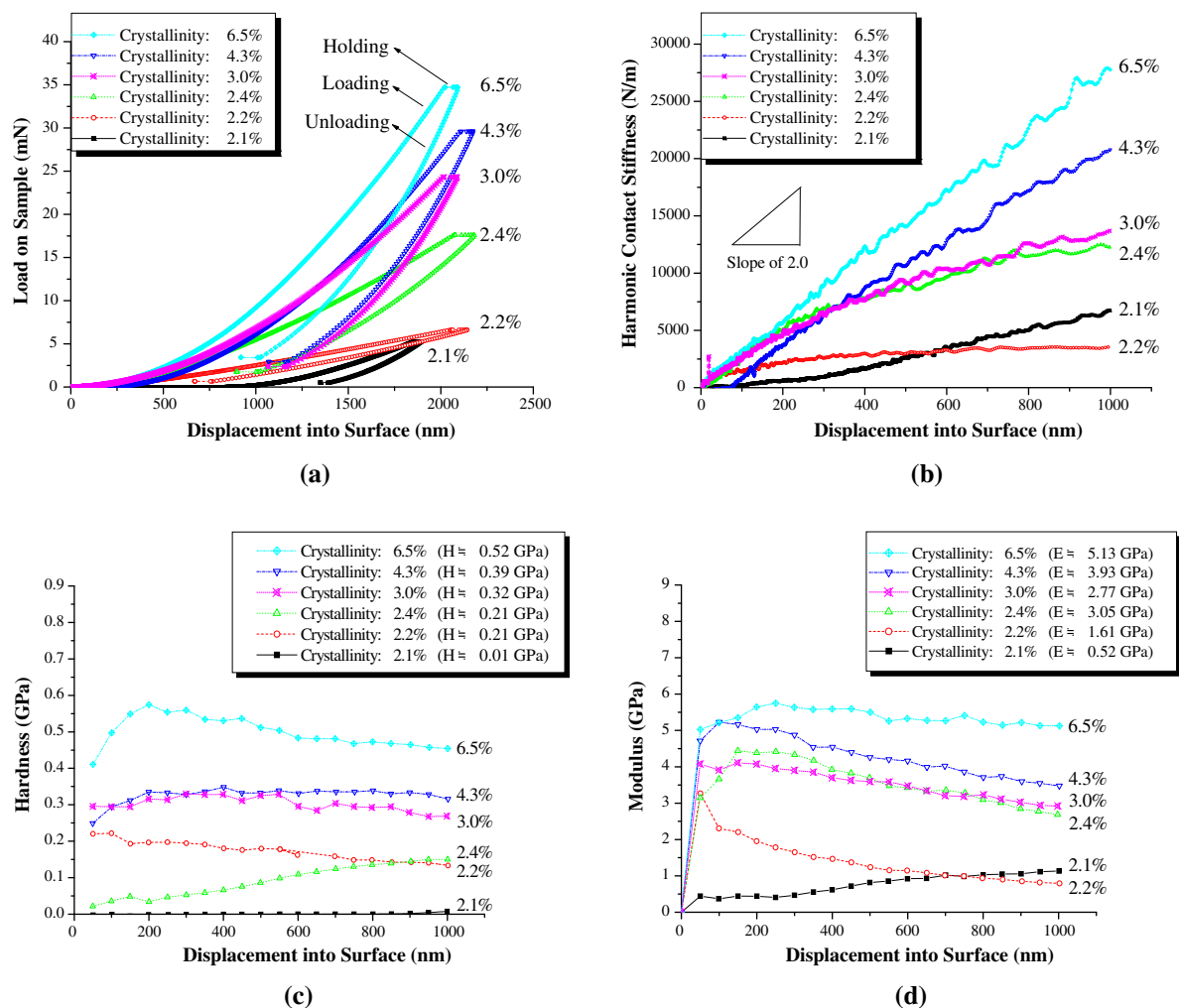

Fig. 9. (a) Load on sample, (b) harmonic contact stiffness, (c) hardness, and (d) modulus vs. the displacement into the surface of **BPAPC-i** fibers with various degrees of crystallinity.

may be attributed to the shorter length of the ordered chains, which form an imperfect crystal ($T_m \sim 245$ °C) at higher temperatures. However, the degree of crystallinity of **BPAPC-i** nanofibers fabricated at 25 kV and 45 °C was only 1.4%. Thus, a higher operating temperature cannot promote the arrangement of locally parallel chain segments in BPAPC nanofibers.

The wide-angle X-ray diffraction (WXRD) pattern of pure BPAPC shows a broad reflection at an angle of $2\theta = 17°$ corresponding to the amorphous phase [28]. However, as shown in Fig. 7a, two strong reflections were observed in **BPAPC-i** nanofibers at $2\theta = 17.3°$ and 21.9°, which indicates that the crystals at $2\theta = 17.3°$ and 21.9° had a heat resistance of 223 °C. Moreover, the reflection at $2\theta = 17.3°$ of the **BPAPC-i** nanofiber gradually disappeared as the operating temperature increased (see Fig. 7b), which is consistent with IR and MDSC results.

3.4. Mechanical properties of BPAPC nanofibers

3.4.1. Nanoscale three-point bend test

To further investigate the relationship between the conformation, crystallinity, and mechanical properties of BPAPC nanofibers, nanoscale three-point bend tests and elastic–plastic nanoindentation tests were performed via AFM and NI, respectively. Fig. 8 and Table 2 exhibit the plots of the elastic moduli and the diameters of **BPAPC-i** nanofibers with varying degrees of crystallinity. The elastic moduli of **BPAPC-i** nanofibers with a crystallinity of 1.4%, 1.5%, 1.7%, 1.8%, 2.1%, 2.2%, 2.4%, 3.0%, 4.3%, and 6.5% were 1.70×10^{-6}, 9.89×10^{-5}, 1.58×10^{-4}, 1.11×10^{-3}, 0.01, 0.04, 0.52, 2.11, 2.86, and 7.11 GPa, respectively. The elastic modulus of **BPAPC-i** nanofibers with a crystallinity of 6.5% was 7.11 GPa, which is superior to that of fibers produced by traditional electrospinning techniques [10–22]. This result illustrates that the modulus of BPAPC nanofibers was greatly enhanced due to an increase in the number of locally ordered parallel chain segments in BPAPC nanofibers. Although **BPAPC-i** nanofibers with a diameter of 270 nm possessed an elastic modulus of 7.11 GPa, the elastic modulus decreased dramatically as the diameter of the nanofiber increased. In a previous study on poly(L-lactide) nanofibers, it was shown that the modulus was strongly dependent on the sample diameter due to the effects of shear deflection in beams with large diameters [31].

3.4.2. Elastic–plastic nanoindentation

Fig. 9a shows the typical results of loading–unloading cycles for **BPAPC-i** nanofibers spun under different electrostatic fields (5, 10, 15, 20, 25, and 30 kV). As shown in the figure, the maximum displacements ranged between 1800 and 2300 nm, and the peak indentation loads of **BPAPC-i** nanofibers with a crystallinity of 2.1%, 2.2%, 2.4%, 3.0%, 4.3%, and 6.5% were 5, 7, 17, 24, 30, and 35 mN, respectively. Fig. 9b exhibits the harmonic contact stiffness of BPAPC nanofibers at various maximum displacements. **BPAPC-i** nanofibers with a crystallinity of 2.1%, 2.2%, 2.4%, 3.0%, 4.3%, and 6.5% displayed a harmonic contact stiffness of 3500, 7000, 12,500, 13,500, 21,000, and 27,500 N/m, respectively. Lower normal loads are required to induce comparable indenter penetrations into soft polymeric surfaces; thus,

the results illustrated the soft nature of **BPAPC-i** nanofibers with crystallinities <2.1%. The hardness of BPAPC nanofibers was evaluated at different maximum contact displacements, and normal indentation experiments were performed at a constant loading, hold, and unloading time. The hardness was evaluated by applying the corrected area function of a silica indenter, which includes a zero-error correction. The mean hardness of **BPAPC-i** nanofibers with a crystallinity of 2.1%, 2.2%, 2.4%, 2.4%, 3.0%, and 6.5% were 0.01, 0.21, 0.21, 0.32, 0.39, and 0.52 GPa, respectively (see Fig. 9c). Moreover, the mean modulus of **BPAPC-i** nanofibers with a crystallinity of 2.1%, 2.2%, 2.4%, 3.0%, 4.3%, and 6.5% were 0.52, 1.61, 3.05, 2.77, 3.93, and 5.13 GPa, respectively (see Fig. 9d). The NI results indicated that the elastic modulus of a **BPAPC-i** nanofiber with a crystallinity of 6.5% was 5.13 GPa. Overall, the results of NI tests were consistent with the AFM results and literature reports [51,52]. Moreover, the elastic modulus of BPAPC nanofibers at 7.11 or 5.13 GPa was superior to that of bulk PC sheets (2–2.4 GPa) or other materials containing PC (1.9 GPa) [10–22].

In summary, the orientation of locally parallel chain segments in BPAPC nanofibers can be induced by conducting an electrospinning process with an additional centrifugal field (1800 rpm). The increased crystallinity can substantially improve the mechanical behavior of BPAPC nanofibers, allowing their future application for the reinforcement of composites.

4. Conclusions

Partially crystalline BPAPC nanofibers were successfully fabricated via electrospinning in an electrostatic field of 25 kV and an additional centrifugal field of 1800 rpm. The results indicated that the maximum crystallinity of BPAPC nanofibers produced via electrospinning was 6.5%. Moreover, as measured by AFM and NI, the elastic modulus of BPAPC nanofibers with a crystallinity of 6.5% was 7.11 and 5.13 GPa, respectively. Thus, the results of this study indicated that the elastic modulus of BPAPC nanofibers was superior to that of BPAPC materials fabricated via conventional processes.

Appendix A. Supplementary data

Supplementary data associated with this article can be found, in the online version, at doi:10.1016/j.eurpolymj.2011.01.006.

References

[1] Tan EPS, Lim CT. Mechanical characterization of nanofibers – a review. Compos Sci Technol 2006;66(9):1102–11.
[2] Bhattarai SR, Bhattarai N, Yi HK, Hwang PH, Cha DI, Kim HY. Novel biodegradable electrospun membrane: scaffold for tissue engineering. Biomaterials 2004;25(13):2595–602.

MACROMOLECULAR NANOTECHNOLOGY

[3] Suthar A, Chase G. Nanofibres in filter media. Chem Eng 2001;726:26–8.

[4] Chatterjee A, Deopura BL. Carbon nanotubes and nanofibre: an overview. Fiber Polym 2002;3(4):134–9.

[5] Bergshoef MM, Vancso GJ. Transparent nanocomposites with ultrathin, electrospun nylon-4, 6 fiber reinforcement. Adv Mater 1999;11(16):1362–5.

[6] Neppalli R, Marega C, Marigo A, Bajgai MP, Kim HY, Causin V. Poly(ε-caprolactone) filled with electrospun nylon fibres: a model for a facile composite fabrication. Eur Polym J 2010;46(5):968–76.

[7] Sundararajan S, Bhushan B, Namazu T, Isono Y. Mechanical property measurements of nanoscale structures using an atomic force microscope. Ultramicroscopy 2002;91(1–4):111–8.

[8] Huanga Z-M, Zhang Y-Z, Kotaki M, Ramakrishna S. A review on polymer nanofibers by electrospinning and their applications in nanocomposites. Compos Sci Technol 2003;63(15):2223–53.

[9] Teo WE, Ramakrishna S. A review on electrospinning design and nanofibre assemblies. Nanotechnology 2006;17(14):89–106.

[10] Krishnappa RVN, Desai K, Sung C. Morphological study of electrospun polycarbonates as a function of the solvent and processing voltage. J Mater Sci 2003;38(11):2357–65.

[11] Tsai PP, Chen WW, Roth JR. Investigation of the fiber, bulk, and surface properties of meltblown and electrospun polymeric fabrics. Inter Nonwoven J 2004;13(3):17–23.

[12] Viswanathamurthi P, Bhattarai N, Kim HY, Cha DI, Lee DR. Preparation and morphology of palladium oxide fibers via electrospinning. Mater Lett 2004;58(26):3368–72.

[13] Shawon J, Sung C. Electrospinning of polycarbonate nanofibers with solvent mixtures THF and DMF. J Mater Sci 2004;39(14):4605–13.

[14] Kattamuri N, Sung C. Uniform polycarbonate nanofibers produced by electrospinning. NSTI-Nanotech 2004;3:425–8.

[15] Wei M, Lee J, Kang B, Mead J. Preparation of core-sheath nanofibers from conducting polymer blends. Macromol Rapid Commun 2005;26(14):1127–32.

[16] Meechaisue C, Dubin R, Supaphol P, Hoven VP, Kohn J. Electrospun mat of tyrosine-derived polycarbonate fibers for potential use as tissue scaffolding material. J Biomater Sci Polymer Ed 2006;17(9):1039–56.

[17] Wei M, Kang B, Sung C, Mead J. Core-sheath structure in electrospun nanofibers from polymer blends. Macromol Mater Eng 2006;291(11):1307–14.

[18] Han X-J, Huang Z-M, He C-L, Liu L, Wu Q-S. Coaxial electrospinning of PC(shell)/PU(core) composite nanofibers for textile application. Polym Composite 2006;27(4):381–7.

[19] Welle A, Kröger M, Döring M, Niederer K, Pindel E, Chronakis IS. Electrospun aliphatic polycarbonates as tailored tissue scaffold materials. Biomaterials 2007;28(13):2211–9.

[20] Kim SJ, Nam YS, Rhee DM, Park H-S, Park WH. Preparation and characterization of antimicrobial polycarbonate nanofibrous membrane. Eur Polym J 2007;43(8):3146–52.

[21] Sihn S, Kim RY, Huh W, Lee K-H, Roy AK. Improvement of damage resistance in laminated composites with electrospun nano-interlayers. Compos Sci Technol 2008;68(3–4):673–83.

[22] Moon S-C, Farris RJ. The morphology, mechanical properties, and flammability of aligned electrospun polycarbonate (PC) nanofibers. Polym Eng Sci 2008;48(9):1848–54.

[23] Von Falkai Bv, Rellensman W. Kristallisation von polycarbonaten II. Dilatometrische untersuchungen an poly-4,4′-dihydroxidiphenyl-2,2-propan-carbonat. Makromol Chem 1965;88(1):38–53.

[24] Aharoni SM, Sanjeeva Murthy N. Effects of solvent-induced crystallization on the amorphous phase of poly(carbonate of bisphenol A). Inter J Polymeric Mater 1998;42(3–4):275–83.

[25] Fan Z, Shu C, Yu Y, Zaporojtchenko V, Faupel F. Vapor-induced crystallization behavior of bisphenol-A polycarbonate. Polym Eng Sci 2006;46(6):729–34.

[26] Takahashi T, Yonetake K, Koyama K, Kikuchi T. Polycarbonate crystallization by vapor-grown carbon fiber with and without magnetic field. Macromol Rapid Commun 2003;24(13):763–7.

[27] Hu X, Lesser AJ. Enhanced crystallization of bisphenol-A polycarbonate by nano-scale clays in the presence of supercritical carbon dioxide. Polymer 2004;45(7):2333–40.

[28] Yin B, Zhao Y, Yang W, Pan M-M, Yang M-B. Polycarbonate/liquid crystalline polymer blend: crystallization of polycarbonate. Polymer 2006;47(25):8237–40.

[29] Heymans N, Rossum SV. FTIR investigation of structural modifications during low-temperature ageing of polycarbonate. J Mater Sci 2002;37(20):4273–7.

[30] Lee S-H, Tekmen C, Sigmund WM. Three-point bending of electrospun TiO$_2$ nanofibers. Mater Sci Eng A 2005;398(1–2):77–81.

[31] Cheng Q, Wang S, Harper DP. Effects of process and source on elastic modulus of single cellulose fibrils evaluated by atomic force microscopy. Compos Part A 2009;40(5):583–8.

[32] Li X, Gao H-S, Murphy CJ, Caswell KK. Nanoindentation of silver nanowires. Nano Lett 2003;3(11):1495–8.

[33] Li X, Gao H-S, Murphy CJ, Gou L. Nanoindentation of Cu$_2$O nanocubes. Nano Lett 2004;4(10):1903–7.

[34] Oliver WC, Pharr GM. An improved technique for determining hardness and elastic modulus using load and displacement sensing indentation experiments. J Mater Res 1992;7(6):1564–83.

[35] Pharr GM, Bolshakov A. Understanding nanoindentation unloading curves. J Mater Res 2002;17(10):2660–71.

[36] Klein CA. Anisotropy of Young's modulus and Poisson's ratio in diamond. Mat Res Bull 1992;27(12):1407–14.

[37] Grimsditch MH, Ramdas AK. Brillouin scattering in diamond. Phys Rev B 1975;11(8):3139–48.

[38] Hruska CK. Least-squares estimates of the nonlinear constants of piezoelectric crystals. J Appl Phys 1992;72(6):2432–9.

[39] McSkimin HJ, Andreatch JP, Glynn P. The elastic stiffness moduli of diamond. J Appl Phys 1972;43(3):985–7.

[40] Zouboulis ES, Grimsditch M, Ramdas AK, Rodriguez S. Temperature dependence of the elastic moduli of diamond: a Brillouin-scattering study. Phys Rev B 1998;57(5):2889–96.

[41] Liao CC, Hou SS, Wang CC, Cheng CY. Electrospinning fabrication of partially crystalline bisphenol A polycarbonate nanofibers: the effects of molecular motion and conformation in solutions. Polymer 2010;51(13):2887–96.

[42] Shenoy SL, Bates WD, Frisch HL, Wnek GE. Role of chain entanglements on fiber formation during electrospinning of polymer solutions: good solvent, non-specific polymer–polymer interaction limit. Polymer 2005;46(10):3372–84.

[43] Reneker DH, Yarin AL. Electrospinning jets and polymer nanofibers. Polymer 2008;49(10):2387–425.

[44] Greiner A, Wendorff JH. Electrospinning: a fascinating method for the preparation of ultrathin fibers. Angew Chem Int Ed 2007;46(30):5670–703.

[45] Deitzel M, Kleinmeyer JD, Hirvonen JK, Beck Tan NC. Controlled deposition of electrospun poly(ethylene oxide) fibers. Polymer 2001;42(19):8163–70.

[46] Wang C, Chien HS, Hsu CH, Wang YC, Wang CT, Lu HA. Electrospinning of polyacrylonitrile solutions at elevated temperatures. Macromolecules 2007;40(22):7973–83.

[47] Whitney DR, Yaris R. Local mechanism of phenyl ring π-flips in glassy polycarbonate. Macromolecules 1997;30(6):1741–51.

[48] Dybal J, Schmidt P, Baldrian J, Kratochvíl J. Ordered structures in polycarbonate studied by infrared and Raman spectroscopy, wide-angle X-ray scattering, and differential scanning calorimetry. Macromolecules 1998;31(19):6611–9.

[49] Kakade MV, Givens S, Gardner K, Lee KH, Bruce Chase D, Rabolt JF. Electric field induced orientation of polymer chains in macroscopically aligned electrospun polymer nanofibers. J Am Chem Soc 2007;129(10):2777–82.

[50] Kongkhlang T, Tashiro K, Kotaki M, Chirachanchai S. Electrospinning as a new technique to control the crystal morphology and molecular orientation of polyoxymethylene nanofibers. J Am Chem Soc 2008;130(46):15460–6.

[51] Esrafilzadeh D, Jalili R, Morshed M. Crystalline order and mechanical properties of as-electrospun and post-treated bundles of uniaxially aligned polyacrylonitrile nanofiber. J Appl Polym Sci 2008;110(5):3014–22.

[52] Hou X, Yang X, Zhang L, Waclawik E, Wu S. Stretching-induced crystallinity and orientation to improve the mechanical properties of electrospun PAN nanocomposites. Mater Design 2010;31(4):1726–30.

MACROMOLECULAR NANOTECHNOLOGY